01 Jul 2024

Induction Vacuum Swing Adsorption over Magnetic Sorbent Monoliths and Extrudates for Ethylene/ethane Separation

Khaled Baamran

Usman Shareef

Fateme Rezaei

Missouri University of Science and Technology, rezaeif@mst.edu

Recommended Citation

K. Baamran et al., "Induction Vacuum Swing Adsorption over Magnetic Sorbent Monoliths and Extrudates for Ethylene/ethane Separation," *AIChE Journal*, vol. 70, no. 7, article no. e18401, Wiley; American Institute of Chemical Engineers (AIChE), Jul 2024.

The definitive version is available at https://doi.org/10.1002/aic.18401

Received: 2 November 2023 | Revised: 3 January 2024 | Accepted: 30 January 2024

DOI: 10.1002/aic.18401

RESEARCH ARTICLE

Editor's Choice: Separations: Materials, Devices and Processes

AIChE JOURNAL

Induction vacuum swing adsorption over magnetic sorbent monoliths and extrudates for ethylene/ethane separation

Khaled Baamran[1] | Usman Shareef[2] | Fateme Rezaei[2]

[1]Linda and Bipin Doshi Department of Chemical and Biochemical Engineering, Missouri University of Science and Technology, Rolla, Missouri, USA

[2]Department of Chemical, Environmental and Materials Engineering, University of Miami, Miami, Florida, USA

Correspondence
Fateme Rezaei, Linda and Bipin Doshi Department of Chemical and Biochemical Engineering, Missouri University of Science and Technology, Rolla, Missouri, USA.
Email: rezaeif@miami.edu

Funding information
National Science Foundation, Grant/Award Number: CBET-2232875

Abstract

Electrification of adsorption processes is emerging as an adaptable solution for future gas separations. This study develops magnetic sorbent structures for use in induction vacuum swing adsorption (IVSA) process specifically designed for olefin/paraffin separation. Two sorbents, namely Fe_3O_4/ZIF-7 (ethane-selective) and Fe_3O_4/13X (ethylene-selective) were developed and formulated into extrudates (Fe_{20}/ZIF-7-P) and monoliths (Fe_{20}/13X-M), and tested under different regeneration scenarios, including simultaneous and subsequent induction-evacuation, induction only, and evacuation only. The dynamic adsorption results demonstrated that regeneration under subsequent induction-evacuation improves desorption rate and capability. Under this regeneration scenario, Fe_{20}/ZIF-7-P achieved an ethane desorption rate of 0.24 mmol/g.min, representing a remarkable 37.5% enhancement over the induction-only scenario. Similarly, Fe_{20}/13X-M exhibited an ethylene desorption rate of 0.35 mmol/g.min, indicative of a 34.2% enhancement. Moreover, the IVSA cyclic runs highlighted the excellent regeneration capability and stability of both Fe_{20}/ZIF-7-P and Fe_{20}/13X-M with Fe_{20}/13X-M exhibiting ethylene purity, recovery, and productivity of 99.4%, 99.6%, and 39.9 mol/kg.h, respectively. Overall, these findings underscore the potential of the hybrid induction/vacuum process as an effective technique for achieving efficient regeneration of sorbents in olefin/paraffin separation.

KEYWORDS
13X, C_2H_6/C_2H_4 separation, Fe_3O_4, induction vacuum swing adsorption, ZIF-7

1 | INTRODUCTION

The demand for ethylene (C_2H_4), a crucial raw material in the chemical industry, continues to grow annually, reaching over 170 million tons worldwide.[1,2] The current methods of producing ethylene, such as paraffin dehydrogenation or steam cracking, result in a mixture of ethane (C_2H_6) and ethylene in the final product.[3,4] To separate these two gases, cryogenic high-pressure distillation process is a well-established industrial separation technology, which is costly and energy-intensive due to their similar volatilities and sizes.[5,6] Approximately 10–20% of the total energy consumption is utilized in the cryogenic distillation process to achieve their separation.[6,7]

Therefore, it is imperative to explore alternative separation approaches that can replace cryogenic distillation to meet the energy efficiency and emission reduction requirements.

Adsorption-based gas separation based on temperature swing adsorption (TSA), pressure or vacuum swing adsorption (PSA or VSA), electric swing adsorption (ESA), and magnetic swing adsorption (MISA) holds significant promise as an alternative to the conventional thermally driven distillation on account of high energy efficiency.[8–10] Hybrid processes have also been attempted to overcome some of the deficiencies of the current adsorption swing processes. For example, in the realm of carbon capture, temperature vacuum swing adsorption (TVSA) has emerged as a particularly promising technology on account

of its effectiveness toward both weakly and strongly adsorbed components.[11,12] Moreover, capitalizing on the strengths of both temperature and vacuum swing processes, TVSA could mitigate high energy penalty and long cooling times typically associated with TSA processes, as it leverages the benefits of lower temperatures and vacuum conditions to desorb the adsorbates.[13] The key striking feature of TVSA lies in its ability to achieve high purity levels in the separated gas.

Various TVSA configurations and heating methods have been explored including indirect heating, where the bed is heated via heated fluids or embedded heat exchangers, and electrified heating via resistive, microwave, or induction heating.[9–16] Electrified heating, in particular, offers distinct advantages in terms of energy efficiency and the ability to precisely control the heating profile.[9,15] Moreover, the integration of vacuum in TVSA allows for efficient desorption at relatively lower temperatures compared to TSA, thereby reducing the overall energy footprint of the process. This dual approach not only ensures effective capture but also aligns with the current focus on developing sustainable and energy-efficient gas separation technologies.[11] For example, Grande and colleagues reported a combined vacuum and electric swing adsorption (VESA) process for CO_2 capture that aimed at improving both CO_2 purity and recovery with a lower regeneration energy.[17] Recently, Denayer group demonstrated the use of a hybrid induction vacuum swing adsorption process (IVSA) for rapid CO_2 desorption, and showed that 90% bed regeneration can be achieved in less than 2 min through a combined induction heating-evacuation process, over 13X zeolite/Fe_3O_4 extrudates.[18]

However, in induction heating, heat is produced uniformly within materials through localized nano-heaters. This technique is particularly suitable for sorbents with low thermal conductivity. By applying high-frequency currents, the magnetic field undergoes changes, leading to the stabilization of eddy currents and the alternating alignment of domains in conductive materials.[9] As a result, the temperature increases, facilitating the regeneration of the sorbent. One benefit of this technology is that it helps minimize heat loss in the adsorption column, which is a problem commonly encountered in TSA. This leads to a reduction in the energy and time required for the cooling step, thereby shortening the overall cycle time. Additionally, heating in MISA is safer than in ESA, as the latter may result in distributed hot spots during heating, which is an advantage of using MISA over ESA.[9,19] However, a significant obstacle arises due to the limited electromagnetic conductivity of the sorbents, making them unresponsive to magnetic fields. To overcome this challenge, researchers have successfully improved the localized thermal heating of sorbent particles by combining magnetic particles with sorbent crystals and utilizing alternating magnetic fields.[9,20–22]

In our earlier works,[19,23] we demonstrated olefin/paraffin separation via MISA process, and our findings highlighted that MISA aids in shortening the cooling step and thereby the cycle time. However, the potential of its dual (hybridized) regeneration mode to further enhance cyclic performance has not yet been demonstrated in olefin/paraffin separation. In terms of sorbent materials, both olefin-selective and paraffin-selective materials have been developed and evaluated for olefin/paraffin separation. Examples of the former class include zeolites,[24,25] γ-Al_2O_3,[26] and metal–organic frameworks (MOFs),[27] whereas for the later class ZIF-7 has been reported.[28] In cases where C_2H_6 is preferentially adsorbed, the desired C_2H_4 product can be directly obtained during adsorption step. This approach offers potential energy savings of around 40% for C_2H_6/C_2H_4 separation compared to using C_2H_4-selective sorbents.[28–30] Nevertheless, its separation factor is currently lower compared to olefin-selective sorbents.[31,32]

In this research, we aimed at utilizing the dual regeneration concept in C_2H_6/C_2H_4 separation by combining evacuation and induction heating in the induction vacuum swing adsorption (IVSA) process, to achieve a rapid desorption rate and a short cycle time. Specifically, we developed two magnetic sorbents, Fe_{20}/ZIF-7-P and Fe_{20}/13X-M with fixed Fe_3O_4 (ca. 20 wt%), which were formulated into extrudates and monolith, respectively, using 3D printing technique.[33] Various induction heating and evacuation scenarios, including simultaneous induction heating and evacuation, as well as individual induction heating or evacuation, were employed to assess the hybridized induction heating and evacuation in the olefin/paraffin separation process. The best regeneration scenario was then selected for cyclic experiments on both sorbents to evaluate their stability and adsorption performance under competitive adsorption. A multicomponent feed containing C_2H_6, C_2H_4, CH_4, and H_2 was used for these experiments to estimate C_2H_4 purity and recovery, along with productivity.

2 | EXPERIMENTAL SECTION

2.1 | Materials

The sorbent synthesis involved the use of various materials, including iron (II, III) oxide microparticles (Fe_3O_4, 99.5%, <5 μm), zinc (II) nitrate hexahydrate ($Zn(NO_3)_2{\cdot}6H_2O$, 99%), benzimidazole, 13X zeolite, bentonite clay (99%), and methylcellulose (99%). These materials were sourced from Sigma Aldrich, except for the 13X zeolite, which was acquired from Alfa Aesar. Additional chemicals, such as methanol (MeOH, 99.9%) and N,N-Dimethylformamide (DMF), were obtained from commercial vendors and used as received without further purification. The ultra-high purity (UHP) gases utilized in this study were purchased from Airgas.

2.2 | Synthesis of magnetic sorbent powders

The preparation of Fe_{20}/13X was carried out following a method described in our recent publication.[19] In a brief summary of the synthesis process, a mixture was prepared by dissolving 20 wt% iron oxide (Fe_{20}) in 50 mL of a 13X/DI water solution. The solution was subjected to rolling at 60 rpm for 24 h. The resulting slurry was then dried at 120 °C for 12 h, and the obtained precipitates were ground to obtain a homogeneous powder using a mortar and pestle. This prepared sample was denoted as Fe_{20} (Fe_3O_4, 30 nm)/13X and referred to as Fe_{20}/13X in the experiments.

The synthesis of ZIF-7 crystals followed established protocols outlined in the available literature.[34,35] To begin, a solid mixture consisting of benzimidazole (0.479 g) and $Zn(NO_3)_2{\cdot}6H_2O$ (0.598 g) was dissolved in 75 mL of DMF and subjected to sonication for 5 min at 25 °C. The resulting solution was then transferred to a Teflon-lined stainless-steel autoclave, where the synthesis process took place without any agitation. The autoclave was placed in an oven and maintained at 120 °C for a duration of 48 h. The solid product was filtered, washed with methanol using vacuum filtration, and subsequently dried under vacuum conditions at 100 °C for 12 h.

2.3 | Formulation of magnetic sorbent structures

The sorbent powders were combined with magnetic particles to create printable inks, with the specific ratios provided in Table 1. These inks were utilized in the 3D printing process to fabricate extrudates of Fe_{20}/ZIF-7 and honeycomb monoliths of Fe_{20}/13X following the methodologies outlined in previous studies.[33,36–40] In summary, the sorbent solids were mixed with bentonite and methylcellulose in a suspension solvent of approximately 20 mL of deionized water (DI) for Fe_{20}/13X or a mixture of DI and MeOH for Fe_{20}/ZIF-7, as shown in Table 1. The mixture of DI and MeOH was used as a solvent in this case because the framework structure of ZIF-7 is known to be sensitive to water. When a sufficient amount of water is used as a solvent, it may cause the ZIF-7 framework to degrade or collapse, resulting in the loss of its desired properties. To avoid this, a mixture of DI water and MeOH is employed as a solvent, as it provides a more suitable environment for synthesizing and handling ZIF-7 without compromising its structural integrity.[35] After combining all components, the ink was subjected to 30 min of sonication and subsequently rolled at 60 rpm for 48 h at 25 °C to ensure homogeneity and promote binding. The resulting slurry was then densified through immersion mixing at 50 °C and 600 rpm until achieving a printable rheology. A printable rheology was defined as being shear thinning and self-standing.[41] The inks were printed using a hydraulic printing setup described in our previous work,[42] followed by drying at 25 °C in a fume hood for 12 h to prevent cracking. Finally, the printed structures were calcined in air at 500 °C for Fe_{20}/13X or at 200 °C for Fe_{20}/ZIF-7 with a ramp rate of 10 °C/min for 5 h. The extrudates/honeycomb monoliths were labeled as Fe_{20}/ZIF-7-P and Fe_{20}/13X-M, as depicted in Figure 1.

TABLE 1 Paste composition of 3D-printed structured sorbents.

Sorbent	Fe_{20}/ZIF-7 or Fe_{20}/13X (wt.%)	Solvent (vol.%)	Bentonite (wt.%)	Methylcellulose (wt.%)
Fe_{20}/ZIF-7	83	H_2O/MeOH (10/90)	14	3
Fe_{20}/13X	83	H_2O	14	3

2.4 | Characterization of magnetics sorbent structures

The textural characteristics of the Fe_{20}/ZIF-7-P and Fe_{20}/13X-M samples were evaluated through N_2 physisorption tests experiments performed at 77 K using a Micromeritics gas analyzer instrument (3Flex). Prior to the analysis, both samples (Fe_{20}/ZIF-7-P and Fe_{20}/13X-M) underwent degassing under vacuum conditions. Fe_{20}/13X-M was degassed at a temperature of 350 °C for 5 h, while Fe_{20}/ZIF-7-P was degassed at 250 °C for the same duration. The degassing process was carried out on a Micromeritics Smart VacPrep instrument. The surface area, pore size distribution (PSD), and pore volume were determined using the Brunauer–Emmett–Teller (BET), Horvath and Kawazoe, and nonlocal density functional theory (NLDFT) methods, respectively. The surface topography was assessed via field emission scanning electron microscopy (FE-SEM; Quanta 600F ESEM). The crystallinity of the synthesized sorbents was assessed via an A PANalytical X'Pert multipurpose X-ray diffractometer with a scan step size of 0.026°/step at a rate of 3°/min from $5° \le 2\theta \le 90°$. It is important to highlight

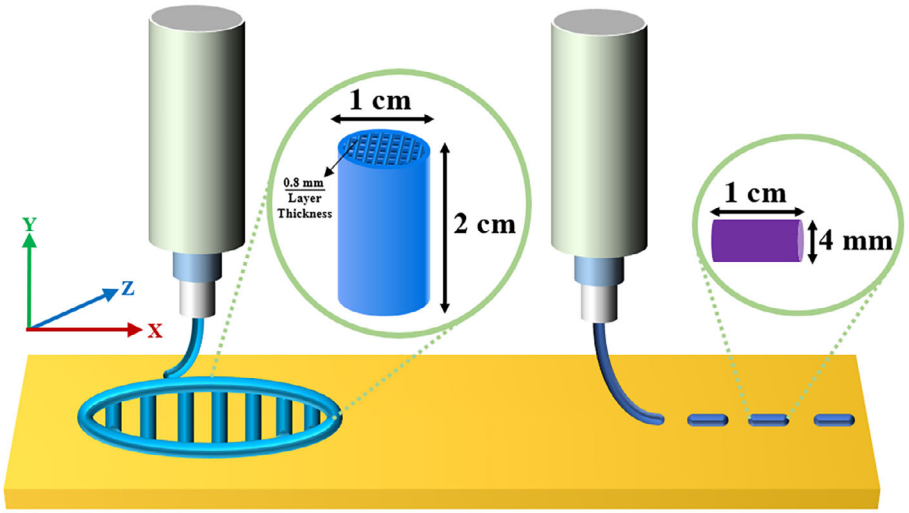

FIGURE 1 Schematic presentation for the formulation of Fe_{20}/ZIF-7-P and Fe_{20}/13X-M structured sorbents.

that the compositions of the iron oxide remained constant in both samples, as previously optimized in our prior works.[19,33] Consequently, the magnetic properties of the Fe_{20}/ZIF-7-P and Fe_{20}/13X-M sorbents, assessed by electron paramagnetic resonance (EPR), specific heat absorption rate (SAR), and heat regeneration requirement calculations, were not presented in this study.

2.5 | Adsorption isotherms measurements

The unary adsorption isotherms of C_2H_6, C_2H_4, CH_4, and H_2 were measured on a volumetric gas analyzer (Micromeritics, 3Flex) within the pressure range of 0–1 bar. Before conducting the measurements, both samples (Fe_{20}/ZIF-7-P and Fe_{20}/13X-M) were subjected to degassing on a Micromeritics Smart VacPrep instrument under vacuum. Fe_{20}/13X-M was degassed at 350 °C for 5 h, while Fe_{20}/ZIF-7-P was degassed at 250 °C for the same duration. This step was carried out to remove any preadsorbed gases or moisture from the samples.

2.6 | Magnetic induction breakthrough experiments

Dynamic adsorption–desorption experiments were carried out using a custom-designed laboratory setup, following the methodology outlined in our previous publications.[19,33,43] The setup involved a quartz tube with dimensions of 25 cm in length and 1 cm in inner diameter. To minimize heat loss, nonconductive plastic materials were chosen for the fittings and connectors of the inlet and outlet openings of the column, as metallic components are susceptible to heating effects during induction heating. The magnetic field strengths applied to the sorbents were generated by an induction heating system (EASYHEAT 1.2 to 2.4 kW-AMBRELL), equipped with an induction coil measuring 4 cm in length, featuring 8 turns and a diameter of 2.5 cm. Throughout each experimental run, precise temperature measurements were ensured by employing a temperature controller (FOTEMP4-PLUS-P0-V-B) in conjunction with a fiber-optic (FO) temperature sensor (OPTOCON, TS3-10MM-02). The breakthrough experiments were conducted under typical operating conditions, including a sorbent mass of 3.0 g, an initial temperature of 25 °C, and a pressure of 1 bar. The adsorption bed was sandwiched between two layers of glass wools, while the remainder of the column was filled with glass beads. Printing a 4 cm monolith could lead to deformation of the monolith because of the adsorption column's narrow diameter (1 cm). A preferable approach would be to print two segments (~2 cm length each) and stack them to constitute the necessary adsorption bed. Prior to the breakthrough experiments, in-situ activation of the sorbent was carried out for 1 h under an Ar flow rate of 20 mL/min, utilizing magnetic field strengths of 31.4 mT for Fe_{20}/13X-M and 21.4 mT for Fe_{20}/ZIF-7-P (the magnetic field strengths of 31.4 and 21.4 mT are equivalent to 250 and 175 A, respectively). After that, the adsorption column was cooled down to 25 °C using compressed air, and a gas mixture of C_2H_6 and C_2H_4 with a feed composition of 50/50 mol% was introduced into the bed at a rate of 54 mL/min, accompanied by a simultaneous flow of 5 mL/min of Ar. It should be noted here that the bed was cooled down by passing the air flow across the column. The gas flow rates at the inlets and outlets were accurately controlled by mass flow controllers (MFCs). The composition of the outlet gas flow was analyzed with using a mass spectrometer (MKS, Cirrus 2). Once the bed reached saturation (ca. pseudo-equilibrium) with C_2H_6 and C_2H_4, the flow of C_2H_6 and C_2H_4 was halted, and the Ar inlet feed was switched to 20 mL/min while activating the sorbent using different magnetic field strengths (31.4 mT for Fe_{20}/13X-M and 21.4 mT for Fe_{20}/ZIF-7-P) at six different scenarios, as illustrated in Figure 2 and Table 2. The desorption process continued until the sorbent bed was fully regenerated from C_2H_6 and C_2H_4.

2.7 | Induction vacuum swing adsorption cyclic experiments

For IVSA experiments, the same adsorption setup was utilized. However, an additional vacuum pump (0.8 and 2 mbar, VACUUBRAND, Germany) was introduced at the outlet of the adsorption column, which was equipped with a bypass for sorbent regeneration runs. These regeneration runs were performed using six different scenarios, as summarized in Table 2. In cyclic adsorption–desorption experiments, the same procedures were repeated for multiple cycles using the best sorbent regeneration scenario, "Indc1-Vac(2)" with varying feed composition to investigate its performance in a competitive adsorption environment, as depicted in Figure 3. The feed gas mixture considered in this study contained C_2H_6, C_2H_4 CH_4, and H_2. The reported flow rate represents the optimal value, as altering the flow rates would yield different gas compositions. For these experiments, a gas mixture of C_2H_6 and C_2H_4 with a feed composition of 13.6/13.6 mol% was introduced into the bed at a flow rate of 15 mL/min. Simultaneously, there was a flow of CH_4/H_2 at 40 mL/min with a feed composition of 14.5/58.2 mol%. The desorption step was carried out until complete regeneration of the sorbent was achieved. Afterward, the system was cooled down to 25 °C before initiating the next cycle. It is worth noting here that during the desorption process, the column was purged with Ar at a flow rate of 20 mL/min. This step served as a desorption step and an activation for the sorbent before starting the subsequent cycle.

3 | RESULTS AND DISCUSSION

3.1 | Characterization of magnetic sorbent structures

The prepared magnetic sorbents were first analyzed by XRD to determine whether the correct crystalline structure was obtained and retained during monolith/extrudates formulation, as shown in Figure S1A,B. First, the diffraction peaks of the ZIF-7 powder, as shown in Figure S1A, were identical to those reported in the

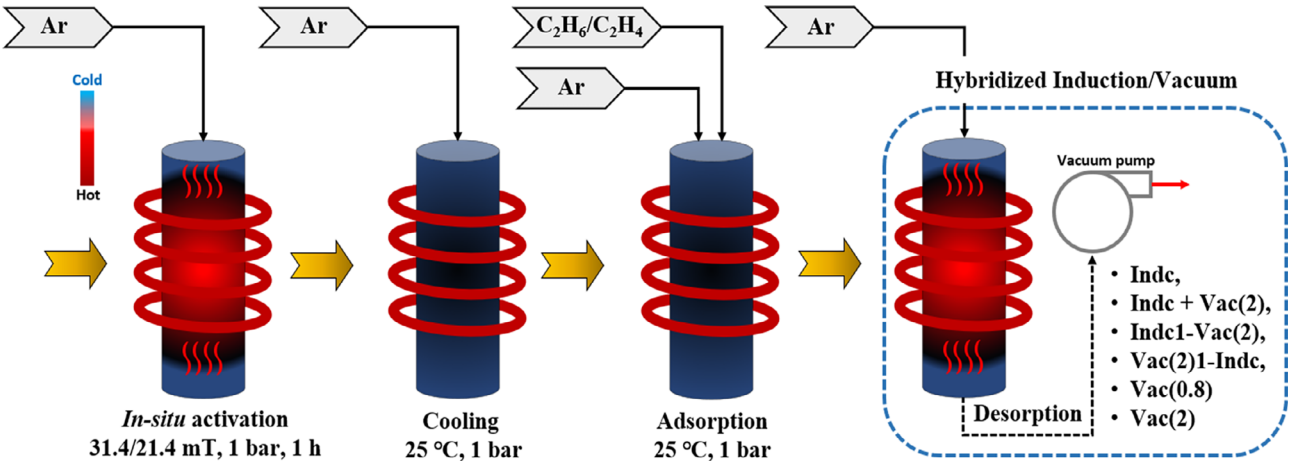

FIGURE 2 Steps of combined magnetic induction heating and vacuum in the process of olefin/paraffin separation for rapid desorption.

TABLE 2 The sequence of different desorption scenarios for sorbent regeneration in the process of induction vacuum swing adsorption.

Sorbent	Run #	Sample activation	Adsorption	Desorption scenario	Symbol of desorption scenario
Fe_{20}/ZIF-7-P	1	21.4 mT 1 h	25 °C 1 bar	Induction	Indc
	2			Induction + Vacuum (2 mbar)	Indc + Vac (2)
	3			Induction (1 min), Vacuum (2 mbar)	Indc1-Vac (2)
	4			Vacuum (2 mbar, 1 min), Induction	Vac (2)1-Indc
	5			Vacuum (0.8 mbar)	Vac (0.8)
	6			Vacuum (2 mbar)	Vac (2)
Fe_{20}/13X-M	1	31.4 mT 1 h	25 °C 1 bar	Induction	Indc
	2			Induction + Vacuum (2 mbar)	Indc + Vac (2)
	3			Induction (1 min), Vacuum (2 mbar)	Indc1-Vac (2)
	4			Vacuum (2 mbar, 1 min), Induction	Vac (2)1-Indc
	5			Vacuum (0.8 mbar)	Vac (0.8)
	6			Vacuum (2 mbar)	Vac (2)

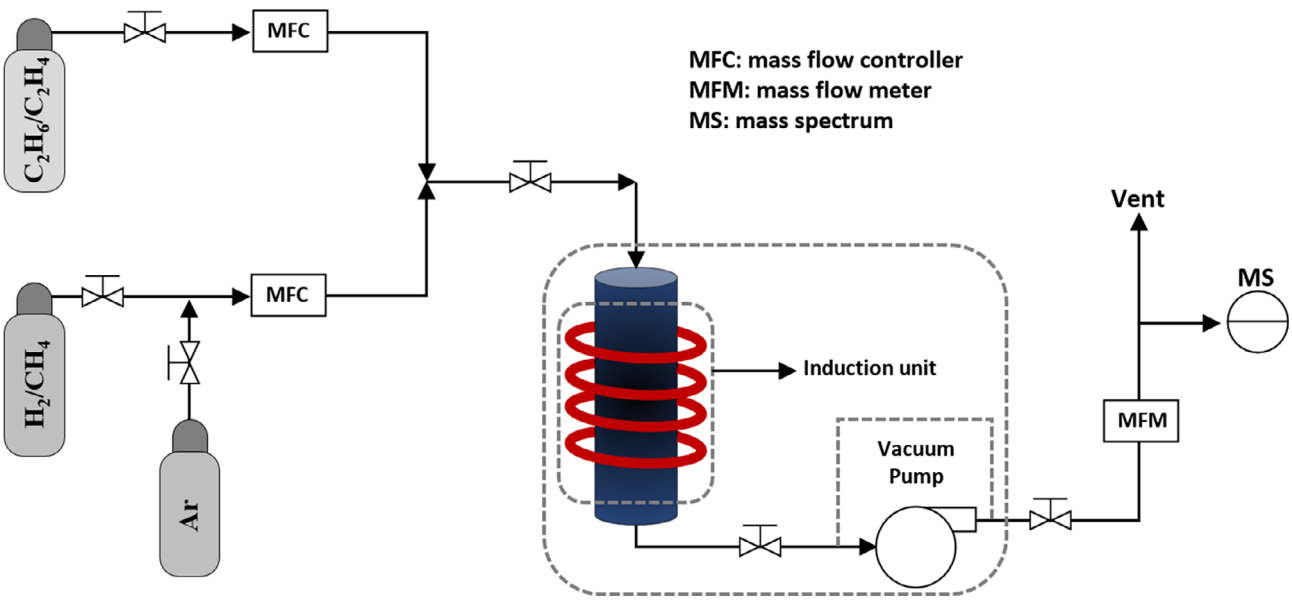

FIGURE 3 Experimental setup used for induction vacuum swing adsorption experiments.

literature,[44–46] indicating the successful synthesis of ZIF-7. Similarly for 13X, the peaks appeared identical to those reported in the literature,[47,48] which was expected as the 13X was used without any modifications. After the addition of magnetic particles (Fe_3O_4), and once the samples were formulated into monoliths or extrudates, the main peaks in both samples were clearly retained, albeit with some reduction in their intensity, in particular for Fe_{20}/ZIF-7-P, indicating strong retention of the crystal structure in Fe_{20}/13X-M and minimal deformation of the crystal structure in formulated structures. The main peaks of Fe_3O_4 were observed at $2\theta = 30.1°$, 37.15°, 43.4°, 53.8°, 57.5°, and 62.5°, corresponding to the crystal planes of (220), (311), (222), (400), (422), (511), and (440), respectively.[49,50] It can be reasonably deduced that Fe_{20}/ZIF-7-P and Fe_{20}/13X-M composites were successfully synthesized. Moreover, these XRD patterns confirmed the presence of both magnetic and sorbent (ZIF-7 or 13X) particles in these composites.

SEM images of the bare sorbents and the composite structures are displayed in Figure S2A–D. Initially examining the bare sorbents, the particles in both samples exhibited an octahedral structure with a nearly round shape, aligning with the typical crystallinity state of ZIF-7 and 13X.[44,47] The synthesized Fe_{20}/ZIF-7-P demonstrated good crystallinity, featuring a uniform distribution of Fe species within the ZIF-7 crystals. However, the crystalline structure of these particles, characterized by a nearly round shape with small crystals, was slightly impacted by the extrusion process, resulting in minor deformation of some ZIF-7 crystals. Nevertheless, the primary crystalline state of ZIF-7 particles was still observable. In contrast, Fe_{20}/13X-M showed no significant alteration to the crystalline structure of the pristine 13X particles, maintaining a uniform distribution of Fe species. These SEM images, in conjunction with the previously discussed XRD data, confirm the successful synthesis of composite materials comprising Fe_3O_4 with ZIF-7 or 13X sorbents. Furthermore, they indicate that the formulation process had a minimal impact on the crystalline structure of the particles, although the ZIF-7 sample exhibited slightly more structural deformation compared to the 13X sample.

The N_2 physisorption isotherms and PSD profiles of the Fe_{20}/ZIF-7-P and Fe_{20}/13X-M sorbents are presented in Figure S3, and the corresponding textural properties can be found in Table S1. Fe_{20}/ZIF-7-P sorbent exhibited a complex N_2 adsorption–desorption isotherm (Figure S3A,B). This behavior can be attributed to the lack of a gate-opening mechanism at low pressure, resulting in limited accessibility of its pores to N_2 molecules.[51,52] This unusual trend in the N_2 physisorption isotherms and the corresponding PSD curve of ZIF-7 aligns with previously reported findings by Cuadrado-Collados et al.[53] and Thakkar et al.[35] On the other hand, the Fe_{20}/13X-M sorbent displayed Type I-IV isotherms (Figure S3C), indicating the presence of a microporous-mesoporous structure. These isotherm types suggest a broader range of pore sizes compared to Fe_{20}/ZIF-7-P. The PSD profiles in Figure S3D confirmed the existence of both micro- and mesopores, spanning a range of 2–30 nm, for these sorbents.

Table S1 presents the BET surface areas and pore volume values for Fe_{20}/ZIF-7-P, which are 18.77 m^2/g and 0.0055 cm^3/g, respectively. While these values may appear relatively low, they are consistent with the findings reported in the literature. It is well-documented that ZIF-7 exhibits limited accessibility for N_2 molecules at 77 K, as previously mentioned. For instance, Cuadrado-Collados et al.[53] and Thakkar et al.[35] reported surface areas of less than 20 m^2/g and total pore volumes of approximately 0.01 cm^3/g for their DMF-based ZIF-7 samples. It should be noted that our Fe_{20}/ZIF-7-P sample contains 20 wt.% of iron oxide, a nonporous material as demonstrated in our previous study.[19] Thus, considering the hybridization with nonporous iron oxide, the obtained surface area and pore volume in Fe_{20}/ZIF-7-P align well with the available literature data. Regarding Fe_{20}/13X-M, the measured BET surface area and total pore volume were found to be 603.4 m^2/g and 0.268 cm^3/g, respectively. These values were slightly lower than those reported in our previous work,[19] where we observed surface areas of 632 m^2/g and total pore volumes of 0.332 cm^3/g for Fe_{20}/13X. This reduction in surface area and porosity can be attributed to the binder used during printing of Fe_{20}/13X-M, given that Fe_{20}/13X-M contains 83% Fe_{20}/13X, as indicated in Table 1. In summary, the obtained surface areas and pore volumes for Fe_{20}/ZIF-7-P and Fe_{20}/13X-M, despite the incorporation of nonporous iron oxide, are still high enough for use in separation processes.

3.2 | Unary adsorption isotherms

The unary adsorption isotherms of C_2H_6, C_2H_4, CH_4, and H_2 were measured at 25 °C over a pressure range of 0–1 bar. These results are illustrated in Figure S4A-D. Upon examining Fe_{20}/ZIF-7-P, an isotherm that appeared to be a combination of Type-IV and S-shaped was observed for C_2H_6, C_2H_4, and CH_4, as depicted in Figure S4. This observation aligns with previously reported results in the literature.[28,35] This material exhibited isotherms consistent with the gate-opening-like effect observed in ZIF-7 topology. This trend can be categorized into three regions: a low-pressure region with minimal gas uptake, indicating weak interaction and external surface adsorption; a step region showing rapid gas uptake within a narrow pressure range, indicative of strong adsorption inside the cavities; and a further filling region where the uptake continues at a more gradual rate, suggesting additional adsorption within the existing cavities. Notably, a steep rise in ethane uptake was observed between 0.10 and 0.20 bar, which can be attributed to the opening of the benzimidazole linker's six-membered ring, leading to rapid cavity filling. This rise became broader with C_2H_4 and CH_4, while minimal adsorption of H_2 was observed. The interaction between adsorbate and linker, influenced by molecular mass, resulted in specific threshold pressures controlling the uptake and release of molecules, allowing C_2H_6 with a larger molecule to adsorb while C_2H_4 and CH_4 did not.[28] The total uptakes over Fe_{20}/ZIF-7-P were 1.93, 1.85, 1.10, and 0.07 mmol/g, for C_2H_6, C_2H_4, CH_4, and H_2, respectively. In contrast to Fe_{20}/ZIF-7-P, Fe_{20}/13X-M exhibited a higher affinity toward C_2H_4 compared to C_2H_6, and even more so over CH_4 and H_2. The isotherms of Fe_{20}/13X-M showed a steep increase in uptake at low pressures, followed by a gradual

increase at higher pressures, while the CH_4 and H_2 isotherms exhibited a gradual increase over the entire pressure range. Notably, the adsorption capacities of CH_4 and H_2 were lower than that of C_2H_4, indicating the selectivity of this sorbent toward C_2H_4 over C_2H_6, and even more pronounced selectivity toward CH_4 and H_2. This selective adsorption can be attributed to π-ion interactions between π bonds of C_2H_4 and electropositive cations (ca. Na^+) in 13X. The Fe_{20}/13X-M material achieved total uptakes of 2.63, 3.15, 2.40, and 0.06 mmol/g for C_2H_6, C_2H_4, CH_4, and H_2, respectively.

3.3 | Induction vacuum breakthrough experiments

3.3.1 | Dynamic adsorption breakthrough

To evaluate the separation performance of the developed sorbents, breakthrough experiments were conducted using a binary gas mixture containing equimolar concentrations of C_2H_6 and C_2H_4. The dynamic concentration profiles for Fe_{20}/ZIF-7-P and Fe_{20}/13X-M sorbents were recorded, as shown in Figure S5A,B. It is important to note here that the term "equimolar" applies to C_2H_6 and C_2H_4 but excludes Ar. Fe_{20}/ZIF-7-P exhibited preferential adsorption of C_2H_6 over C_2H_4, but with lower C_2H_6/C_2H_4 than that of pristine ZIF-7, likely due to the inclusion of nonporous iron oxide and the mixing with binders/solvents during the extrusion process, which affected its overall separation efficiency. Despite low selectivity, the separation between these two gases was validated from the breakthrough profiles, indicating that Fe_{20}/ZIF-7-P still retains the inherent properties of ZIF-7. The concentration fronts revealed an overshoot in the C_2H_4 wavefront, which occurred due to breakthrough of C_2H_6 from the outlet of the bed. This overshoot was caused by the displacement of weaker adsorbate molecules of C_2H_4 by the stronger adsorbate molecules of C_2H_6, resulting in concentrations exceeding the relative concentration of $C_i/C_0 = 1$. As C_2H_6 neared the end of the column, the gas mixture reached a state of binary saturation, causing both C_2H_6 and C_2H_4 to return to their original molar feed compositions. Similarly, in the case of Fe_{20}/13X-M, a similar trend was observed where the wavefront of the lighter gas was displaced by the stronger adsorbate molecules. However, the gas selectivity of Fe_{20}/13X-M was opposite to that of Fe_{20}/ZIF-7-P. This difference in selectivity can be attributed to the distinct adsorption mechanisms, as discussed earlier. In the case of Fe_{20}/ZIF-7-P, the adsorption mechanism was likely reliant on the gate-opening mechanism in ZIF-7, as indicated by the adsorption isotherms, which were also similar to those reported in the literature.[28] This effect is influenced by the molecular mass of the adsorbate and involves specific threshold pressure that controls the uptake and release of molecules. Consequently, C_2H_6, being the larger molecule, is adsorbed, while C_2H_4 does not exhibit significant adsorption. In contrast, the adsorption mechanism in Fe_{20}/13X-M is based on π-ion interactions between the π bonds of C_2H_4 and electropositive cations (ca. Na^+) in 13X, resulting in 13X preferentially adsorbing C_2H_4 over C_2H_6.[54,55]

3.3.2 | Bed regeneration scenarios

The desorption rate is significantly influenced by the varying driving forces, particularly when utilizing heating and vacuum techniques. However, achieving a desired desorption rate at lower temperatures is crucial, as it effectively reduces cooling step and overall cycle times. While evacuation is a feasible method to obtain a high desorption rate at low temperatures, it comes with the drawback of requiring the vacuum pump to operate at very low pressures, resulting in higher costs. To address this, a promising approach is to develop a hybrid system that combines heating and evacuation at moderate temperature and pressure conditions, aiming to lower the energy regeneration requirements associated with both methods. Thus, the study explores six different regeneration scenarios, as illustrated in Table 2, to determine the most efficient combination for enhanced desorption performance.

In the "Vac(2)" scenario, which relies solely on pressure reduction as the driving force for regeneration, rapid desorption was observed initially, followed by a slower desorption rate, as depicted in Figure 4A. During the initial 2–3 min, a steep decline in ethane desorption was noted, likely due to the presence of weakly adsorbed ethane molecules. Over time, however, the desorption curve stabilized, and the regeneration took longer to complete. This behavior can be attributed to the steep isotherms observed for Fe_{20}/ZIF-7-P at low C_2H_6 partial pressures, posing a challenge for rapid regeneration when using vacuum alone. It is also worth noting that the suction capacity of the vacuum pump decreases significantly at very high vacuum levels. Consequently, the pump may struggle to effectively remove the limited number of gas molecules present, thereby reducing its efficiency in evacuating the system, thus contributing to the slowed regeneration process over time.[18] Using the same scenario but at a lower vacuum pressure "Vac(0.8)," a similar trend was observed. However, at this lower pressure, both a higher regeneration ability and a more rapid desorption rate were attained (Figure 5A).

In the "Indc" scenario (Figure 4A), where only induction heating is used, the desorption curve exhibited a broad profile with a slow reduction rate over time. This can be explained by the fact that the strength of magnetic field applied was lower, thus it took longer time to reach the energy level required to weaken the bonds between the molecules and the sorbent. (Figure 5A). However, when induction heating is combined with vacuum ("Indc + Vac(2)" in Figure 4A), the desorption curve of ethane sharpened at the beginning of desorption. This improved desorption rate can be attributed to the synergistic effect of induction heating and vacuum in that induction heating provides the initial energy required to weaken the bonds between the adsorbate molecules and the sorbent, facilitating their detachment, while at the same time, the vacuum environment reduces the pressure around the adsorbate molecules, facilitating their movement away from the sorbent. The combination of these two factors leads to improved desorption rate and regeneration process (Figure 5A).

In the "Indc1-Vac(2)" scenario, induction heating leads to a rapid temperature increase, facilitating initial desorption within 1 min (Figure 4A). However, once the induction heating is interrupted, the

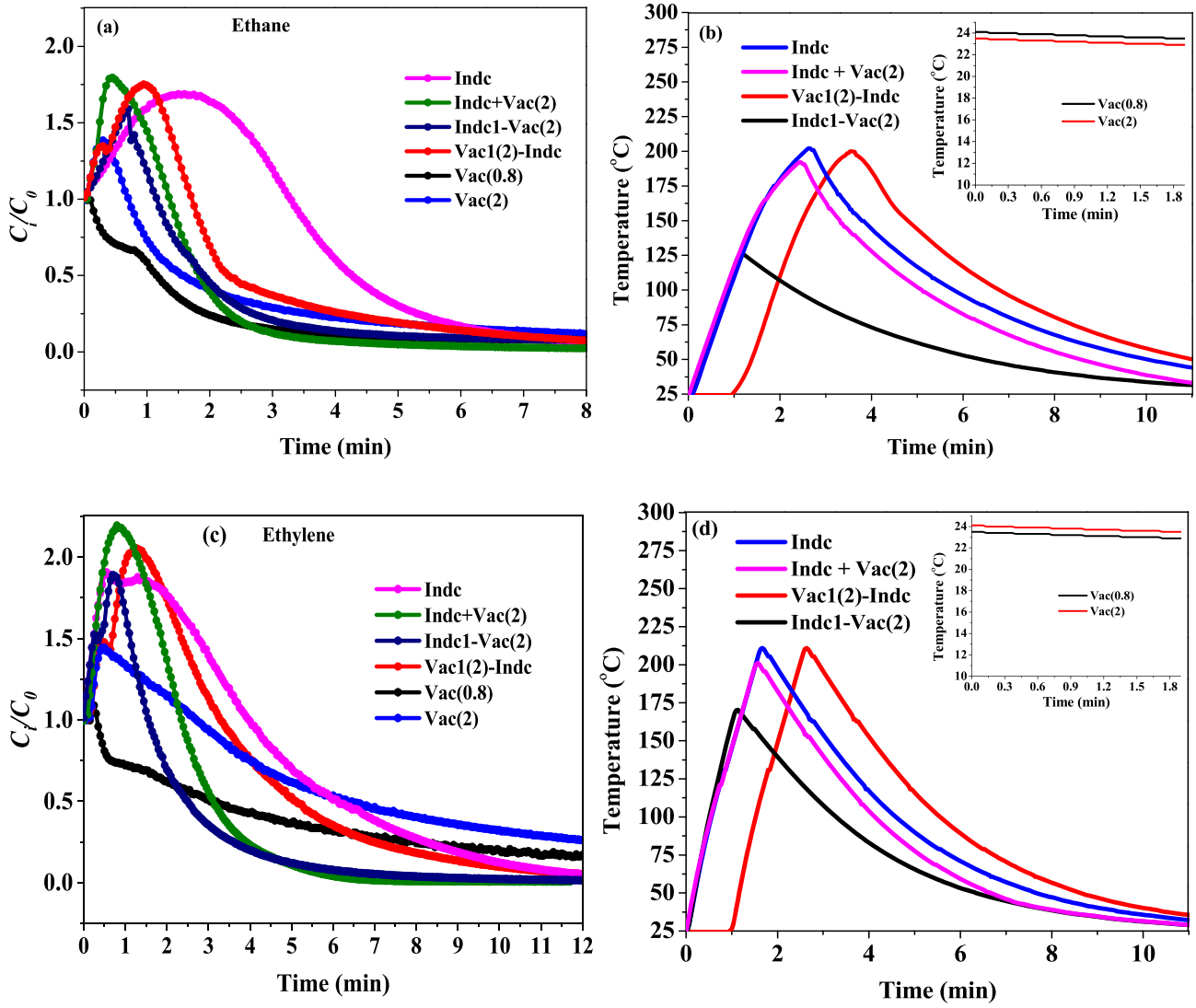

FIGURE 4 Desorption profiles under different regeneration conditions and the corresponding temperature profiles: (A, B) Fe_{20}/ZIF-7-P and (C, D) Fe_{20}/13X-M.

desorption plateau experiences a steep decline. This trend of a rapid decrease in desorption can be explained by analyzing the temperature profile (Figure 4B). When the alternating current is initiated, the temperature rises, and when the current is ceased, the temperature immediately drops without any delay. This fast temperature response is an advantageous feature of induction heating to reduce the cooling time.[19,23,33] It is worth noting that the temperature profile is only reported during the initial minutes of induction or when the temperature reaches 200 °C, due to the temperature sensor's maximum capability of 250 °C, which is implemented to prevent any potential damage to the sensor. The application of vacuum enhances the desorption rate by increasing the driving force, as depicted in Figure 4A. This improved desorption is observed over a time period similar to that of the "Indc + Vac(2)" scenario. This suggests that using a sequential approach of heating followed by evacuation is advantageous. Specifically, reducing the desorption temperature leads to a faster cooling rate, thereby shortening the cycle time. Furthermore, its regeneration ability was closely aligned with what was observed in the "Indc + Vac(2)" scenario. Further reducing the pressure (<2 mbar) in the evacuation step will undoubtedly enhance the desorption of strongly adsorbed molecules, but this enhancement will come at the expense of increasing the energy regeneration costs.[18] As a result, the lowest pressure of the vacuum pump was limited to 2 mbar in the combined scenarios. Similarly, in the "Vac1-Indc" scenario (Figure 4A), the vacuum is utilized to reduce the pressure, aiding in the desorption process by removing weakly adsorbed molecules. This is evident from the small plateau observed in the initial minute of desorption. Subsequently, induction heating was applied, providing the required energy for complete regeneration. This is reflected by the sharp increase in the desorption plateau, as depicted in Figure 4A. This scenario led to a moderate desorption rate and regeneration ability, with an expectedly longer cycle time due to the heating that follows evacuation, which in turn reduces the cooling rate. In contrast, Fe_{20}/13X-M exhibited a different trend in desorption

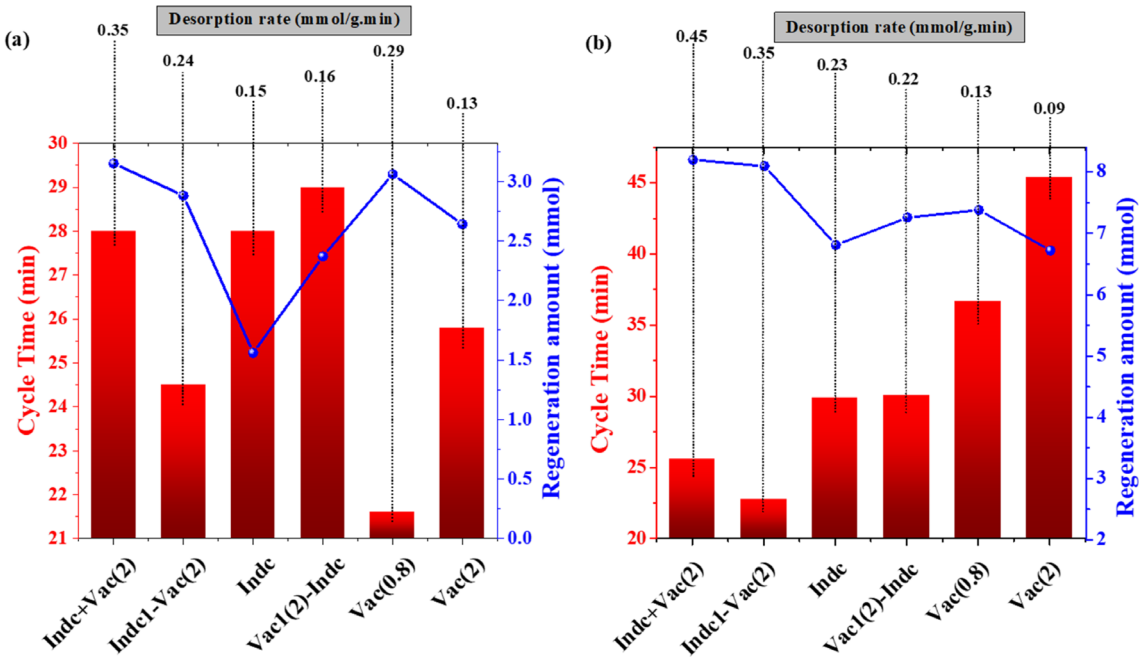

FIGURE 5 Desorption rate, regeneration amount, and cycle time obtained at different regeneration scenarios (A) Fe_{20}/ZIF-7-P (ethane) and (B) Fe_{20}/13X-M (ethylene).

scenarios (Figure 4C), owing to the difference in their adsorption mechanisms and regeneration conditions. However, common trends were observed in both the "Indc1-Vac(2)" and "Indc + Vac(2)" scenarios. The former led to conditions that resulted in a high desorption rate with a shorter cycle time, while the latter led to the best regeneration ability due to the synergistic driving forces applied simultaneously.

To evaluate the regeneration scenarios, different parameters such as desorption rate and capacity, and cycle time were estimated using equation S3–S5, as depicted in Figure 5A,B. The results demonstrate an enhancement in the desorption rate and regeneration amount achieved through the hybridized induction heating/vacuum approach "Indc + Vac(2)" compared to the other scenarios. However, the "Indc1-Vac(2)" mode led to a significant cycle time reduction, with decreases of roughly 12.5% in Fe_{20}/ZIF-7-P and 23.2% in Fe_{20}/13X-M, respectively, compared to the "Indc + Vac(2)" and "Indc." This was achieved while maintaining a high desorption rate and regeneration ability nearly equivalent to that of "Indc + Vac(2)." The desorption rate and regeneration amount were measured at 0.24 mmol/g.min and 2.88 mmol for ethane in Fe_{20}/ZIF-7-P, and 0.35 mmol/g.min and 8.10 mmol for ethylene in Fe_{20}/13X-M, respectively. These desorption rates represent respectively, remarkable 37.5%–45.8% and 34.2%–74.2% enhancements compared to the rates observed in the "Indc" and "Vac(2)" regeneration scenarios for both sorbents. Clearly, the technique employed in the Indc1-Vac (2) scenario successfully adjusted the parameters needed for efficient cyclic separation, establishing "Indc1-Vac(2)" as the most effective regeneration scheme. Overall, these findings underscore the potential of this modified MISA system (IVSA) as a promising technique for achieving efficient regeneration under moderate temperature and pressure conditions, ultimately reducing the overall costs associated with sorbent regeneration.

The *SAR* values in this study remained consistent with what we have recently published, as we utilized the same iron oxide properties (ca. oxide phase, particle size, and ion states). These *SAR* values were among the best reported in the literature thus far.[9,18,20,21] With respect to the desorption rate, it is worth noting that, to the best of our knowledge, there have been no published works that specifically discuss the utilization of the induction heating method in the process of separating light olefins/paraffins by adsorption. While there have been a few studies that have explored this technology as an alternative heating method for sorbent regeneration for CO_2 release, its application in the context of light olefins/paraffins separation remains largely unexplored. By coupling induction and vacuum methods, we were able to achieve a significant enhancement in the desorption rate of ethylene in Fe_{20}/13X-M compared to our previous work.[23] It is worth noting that there is no study in the literature that has investigated the use of Fe_{20}/ZIF-7 as a magnetic sorbent for ethane desorption under magnetic induction heating. These results suggest that the formulated sorbents hold promise for olefin/paraffin separation in the IVSA process. Furthermore, the application of 3D printing technique for the formulation of sorbents provides benefits pertaining to their structural integrity and robustness[56]

3.4 | Cyclic IVSA experiments

Evaluating the performance of sorbents under cyclic conditions is essential for thoroughly assessing their suitability in real applications.

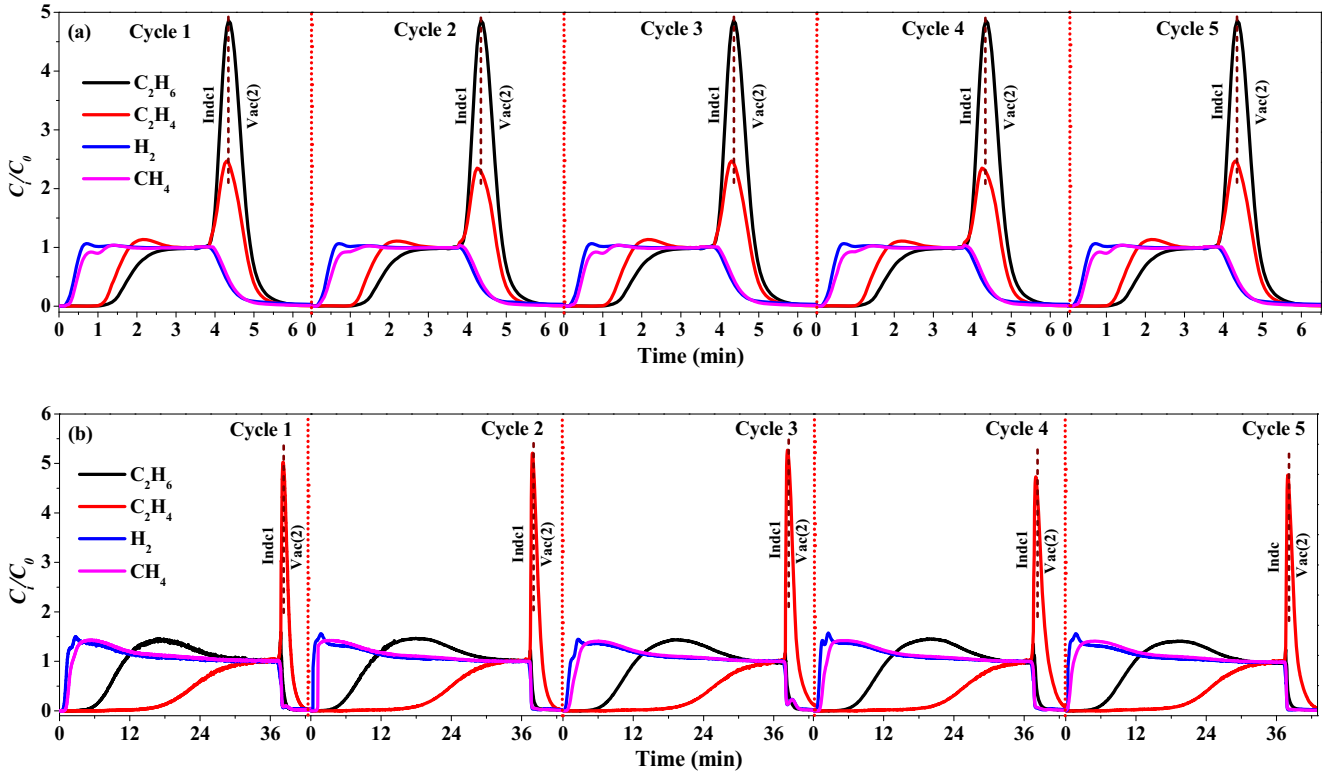

FIGURE 6 Cyclic induction vacuum swing adsorption experiments were conducted on (A) Fe_{20}/ZIF-7-P at 25°C and 1 bar during adsorption, and using the Indc1-Vac(2) scenario during desorption; (B) Fe_{20}/13X-M at 25 °C and 1 bar during adsorption, and using Indc1-Vac(2) scenario during desorption. The transition between heating and evacuation in the desorption curves was removed and smoothed for clarity.

In this study, the cyclic performances of Fe_{20}/ZIF-7-P and Fe_{20}/13X-M were performed at the refined regeneration scenario "Indc1-Vac(2)" and the corresponding results are shown in Figure 6A,B. The investigation involved subjecting the sorbents to five cycles of adsorption–desorption experiments at a temperature of 25 °C and a pressure of 1 bar during the adsorption step. The desorption step was carried out under a magnetic field strength of 21.4 mT for Fe_{20}/ZIF-7-P and 31.4 mT for Fe_{20}/13X-M. The results depicted in Figure 6A,B clearly demonstrate the regeneration capability of both sorbents Fe_{20}/13X-M and Fe_{20}/ZIF-7-P over five cycles, with less durability noticed with the Fe_{20}/ZIF-7-P compared to the Fe_{20}/13X-M, likely due to the more sensitive ZIF structure when mixing with binders/solvents during the extrusion process. However, these findings highlight the excellent separation efficiency and durability of Fe_{20}/13X-M, making it an efficient sorbent for practical implementation in the MISA/IVSA processes. Fe_{20}/ZIF-7-P, on the other hand, exhibited lower separation efficiency, but it still maintained its regeneration activity and ethane selectivity over ethylene. This suggested that while Fe_{20}/ZIF-7-P demonstrated potential for the modified MISA system, its C_2H_6/C_2H_4 selectivity and durability should be further improved, especially under multicomponent feed conditions.

3.5 | Purity, recovery, and productivity

Determination of purity, recovery, and productivity is essential in assessing the performance and efficiency of a system or process. In this study, we focused on estimating the purity, recovery, and productivity of ethylene, as it is the desired gas to be obtained in high purity, using equations S6–S11 in the Supporting Information.

The maximum values of purity, recovery, and productivity for Fe_{20}/ZIF-7-P and Fe_{20}/13X-M are shown in Figure 7A,B. It is evident that despite the variations in performance between these sorbents, they both demonstrated excellent regeneration under the given conditions across five consecutive cycles. However, Fe_{20}/13X-M exhibited higher ethylene purity and productivity compared to ethylene in Fe_{20}/ZIF-7-P. The ethylene purity achieved over Fe_{20}/13X-M and Fe_{20}/ZIF-7-P were found to be 99.40% and 50.58%, respectively, whereas the productivity values were estimated to be 39.87 and 20.22 mol/kg.h, respectively. The differing performance of these sorbents can be attributed to the ethylene/ethane selectivity resulting from their distinct adsorption mechanisms, and heating regeneration (ca. 31.4 mT in Fe_{20}/13X-M and 21.4 mT in Fe_{20}/ZIF-7-P). For Fe_{20}/ZIF-7-P, the ethane adsorption capacity and ethane/ethylene selectivity were measured at 1.05 mmol/g and 1.10, respectively, while for Fe_{20}/13X-M, the ethylene adsorption capacity and ethylene/ethane selectivity were 2.73 mmol/g and 2.55 (Tables S2 and S3), respectively. These results indicate that the purity of ethylene in Fe_{20}/ZIF-7-P is more affected by the presence of adsorbed impurity gases during the adsorption step, which was not the case for Fe_{20}/13X-M. Nevertheless, the results reported in this study represent a promising initial stride toward the advancement of ethane-selective magnetic

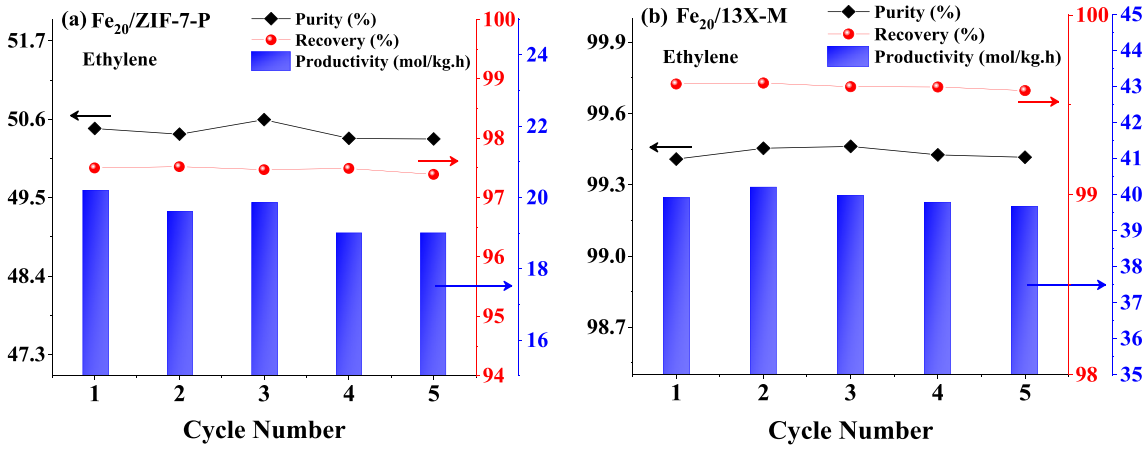

FIGURE 7 The ethylene purity, recovery, and productivity results of (A) Fe_{20}/ZIF-7-P and (B) Fe_{20}/13X-M.

sorbents (ESMS). These findings also suggest that there is a need for further improvement in ethane-selective sorbents to be used in future studies on the MISA process for gas separation. The reason can be attributed to the incorporation of magnetic particles and binders/solvents during the synthesis of ESMS affecting the structure of ZIF-7 and thus the overall adsorption performance.

4 | CONCLUSIONS

Fe_{20}/ZIF-7-P and Fe_{20}/13X-M, two magnetic sorbents with distinct adsorption mechanisms, were developed and studied for their effectiveness in olefin/paraffin separation through a hybridized process of induction heating and evacuation. Six different regeneration scenarios were employed, and the best scenario, labeled as "Indc1-Vac (2)" yielded an improvement in the desorption rate and regeneration ability with a remarkable reduction in the cycle time stemming from a lower bed temperature. Specifically, in the "Indc1-Vac(2)" regeneration scenario, the desorption rates of the heavier adsorbed gases were found to be 0.24 mmol/g.min for ethane in Fe_{20}/ZIF-7-P and 0.35 mmol/g.min for ethylene in Fe_{20}/13X-M. These rates represented notable 37.5%–45.8% and 34.2%–74.2% enhancements, respectively, compared to the desorption rates observed in "Indc" and "Vac(2)" regeneration scenarios. Moreover, this regeneration mode resulted in shortening of cycle time by 12.5% and 23.7% when compared to the sole application of induction heating in Fe_{20}/ZIF-7-P and Fe_{20}/13X-M, respectively. During the "Indc1-Vac(2)" regeneration scenario, both Fe_{20}/ZIF-7-P and Fe_{20}/13X-M underwent five consecutive adsorption–desorption cyclic tests, and the results showcased excellent regeneration capability and durability of Fe_{20}/13X-M. This material outperformed Fe_{20}/ZIF-7-P by achieving ethylene purity, recovery, and productivity of 99.40%, 99.61%, and 39.87 mol/kg.h, respectively. Overall, these findings highlight the potential of the hybridized process of induction/vacuum as an effective technique for achieving efficient regeneration in olefin/paraffin separation.

AUTHOR CONTRIBUTIONS

Khaled Baamran: Investigation (lead); methodology (lead); writing – original draft (lead). **Usman Shareef:** Data curation (supporting); formal analysis (supporting); methodology (supporting). **Fateme Rezaei:** Conceptualization (lead); formal analysis (supporting); funding acquisition (lead); project administration (lead); supervision (equal); writing – review and editing (lead).

ACKNOWLEDGMENTS

The authors acknowledge financial support from National Science Foundation (NSF CBET-2232875).

CONFLICT OF INTEREST STATEMENT

The authors declare that there are no conflicts of interests.

DATA AVAILABILITY STATEMENT

The data that support the findings of this study are available on request from the corresponding author. The numerical data from Figures 4–7 are tabulated in Appendix S1.

ORCID

Fateme Rezaei https://orcid.org/0000-0002-4214-4235

REFERENCES

1. Yue B, Liu S, Chai Y, Wu G, Guan N, Li L. Zeolites for separation: fundamental and application. *J Energy Chem*. 2022;71:288-303. doi:10.1016/j.jechem.2022.03.035
2. Li L, Lin RB, Krishna R, et al. Ethane/ethylene separation in a metal-organic framework with iron-peroxo sites. *Science*. 2018;362(6413):443-446. doi:10.1126/science.aat0586
3. Liu C, Xin M, Wang C, et al. Ag_2O nanoparticles encapsulated in Ag-exchanged LTA zeolites for highly selective separation of ethylene/ethane. *ACS Appl Nano Mater*. 2023;6(7):5374-5383. doi:10.1021/acsanm.2c05296
4. Wu Q, Li G, Cheng Y, et al. Efficient separation of ethylene/ethane by incorporation of silver salts into protic imidazole ionic liquids. *Chem Eng J*. 2023;461:141942. doi:10.1016/j.cej.2023.141942

5. Ren M, Liu W, Li D, et al. Synergistic effect of silver-based ionic liquid for ethylene/ethane separation. *Ind Eng Chem Res*. 2023;62(22):8893-8901. doi:10.1021/acs.iecr.3c00721
6. Yu C, Guo Z, Yang L, et al. A robust metal-organic framework with scalable synthesis and optimal adsorption and desorption for energy-efficient ethylene purification. *Angewandte Chemie*. 2023;135(16):e202218027. doi:10.1002/ange.202218027
7. Liu C, Xin M, Zhang X, Wang C, Qiu L, Xu G. Unraveling separation mechanisms of LTA zeolite depending on regulated particle size and pore structure for efficient ethylene/ethane separation. *New J Chem*. 2023;47:12279-12286. doi:10.1039/D3NJ01217D
8. Al Moinee A, Rownaghi AA, Rezaei F. Challenges and Opportunities in Electrification of Adsorptive Separation Processes. *ACS Energy Lett*. 2024;9(3):1228-1248. doi:10.1021/acsenergylett.3c02340
9. Gholami M, Verougstraete B, Vanoudenhoven R, Baron GV, Van Assche T, Denayer JFM. Induction heating as an alternative electrified heating method for carbon capture process. *Chem Eng J*. 2022;431:133380.
10. Sharma R, Saab G, Schoukens M, Van Assche TRC, Denayer JFM. Ferromagnetic metal organic framework (MOF)/alginate hybrid beads for atmospheric water capture and induction heating-enabled water release. *Appl Mater Today*. 2023;35:101918.
11. Gholami M, Van Assche TRC, Denayer JFM. Temperature vacuum swing, a combined adsorption cycle for carbon capture. *Curr Opin Chem Eng*. 2023;39:100891.
12. Verougstraete B, Martin-Calvo A, Van der Perre S, Baron G, Finsy V, Denayer JFM. A new honeycomb carbon monolith for CO_2 capture by rapid temperature swing adsorption using steam regeneration. *Chem Eng J*. 2020;383:123075.
13. Wurzbacher JA, Gebald C, Steinfeld A. Separation of CO_2 from air by temperature-vacuum swing adsorption using diamine-functionalized silica gel. *Energ Environ Sci*. 2011;4(9):3584-3592.
14. Ejeian M, Wang RZ. Adsorption-based atmospheric water harvesting. *Joule*. 2021;5:1678-1703. doi:10.1016/j.joule.2021.04.005
15. Gomez-Rueda Y, Verougstraete B, Ranga C, Perez-Botella E, Reniers F, Denayer JFM. Rapid temperature swing adsorption using microwave regeneration for carbon capture. *Chem Eng J*. 2022;446:137345.
16. Esmaeili F, Hojjat M, Denayer JFM, Gholami M. CO_2 capture on an adsorbent-coated finned tube heat exchanger: effect of the adsorbent thickness. *ACS Publ*. 2021;60(12):4677-4681. doi:10.1021/acs.iecr.0c06171
17. Zhao Q, Fan W, Men Y, et al. CO_2 capture using a novel hybrid monolith (H-ZSM5/activated carbon) as adsorbent by combined vacuum and electric swing adsorption (VESA). *Chem Eng J*. 2019;358:707-717.
18. Schoukens M, Gholami M, Baron GV, Van Assche T, Denayer JFM. Hybrid induction vacuum swing adsorption, a rapid and fully electrified carbon capture process. *Chem Eng J*. 2023;459:141587. doi:10.1016/j.cej.2023.141587
19. Baamran K, Rownaghi AA, Rezaei F. Magnetic-induced swing adsorption over iron oxide/13X: effects of particle size and oxide phase on sorbent regeneration in ethylene/ethane separation. *ACS Sustain Chem Eng*. 2023;11(23):8603-8614. doi:10.1021/acssuschemeng.3c01468
20. Sadiq MM, Li H, Hill AJ, Falcaro P, Hill MR, Suzuki K. Magnetic induction swing adsorption: an energy efficient route to porous adsorbent regeneration. *Chem Mater*. 2016;28(17):6219-6226. doi:10.1021/acs.chemmater.6b02409
21. Li H, Sadiq MM, Suzuki K, et al. Magnetic metal-organic frameworks for efficient carbon dioxide capture and remote trigger release. *Adv Mater*. 2016;28(9):1839-1844. doi:10.1002/adma.201505320
22. Sadiq MM, Konstas K, Falcaro P, Hill AJ, Suzuki K, Hill MR. Engineered porous nanocomposites that deliver remarkably low carbon capture energy costs. *Cell Rep Phys Sci*. 2020;1(6):100070. doi:10.1016/j.xcrp.2020.100070
23. Baamran K, Newport K, Rownaghi AA, Rezaei F. Development and assessment of magnetic Fe_2O_3@MOF-74 composite sorbents for ethylene/ethane separation. *Chem Eng J*. 2023;451:139006. doi:10.1016/j.cej.2022.139006
24. Aguado S, Bergeret G, Daniel C, Farrusseng D. Absolute molecular sieve separation of ethylene/ethane mixtures with silver zeolite A. *J Am Chem Soc*. 2012;134(36):14635-14637. doi:10.1021/ja305663k
25. Bereciartua PJ, Cantín Á, Corma A, et al. Control of zeolite framework flexibility and pore topology for separation of ethane and ethylene. *Science*. 2017;358(6366):1068-1071. doi:10.1126/science.aao0092
26. Yang RT, Kikkinides ES. New sorbents for olefin/paraffin separations by adsorption via π-complexation. *AIChE J*. 1995;41(3):509-517. doi:10.1002/aic.690410309
27. Gong Y, Chen C, Lively RP, Walton KS. Humid ethylene/ethane separation on ethylene-selective materials. *Ind Eng Chem Res*. 2021;60(27):9940-9947. doi:10.1021/acs.iecr.1c01291
28. Gücüyener C, Van Den Bergh J, Gascon J, Kapteijn F. Ethane/ethene separation turned on its head: selective ethane adsorption on the metal-organic framework ZIF-7 through a gate-opening mechanism. *J Am Chem Soc*. 2010;132(50):17704-17706. doi:10.1021/ja1089765
29. Liao PQ, Zhang WX, Zhang JP, Chen XM. Efficient purification of ethene by an ethane-trapping metal-organic framework. *Nat Commun*. 2015;6(1):1-9. doi:10.1038/ncomms9697
30. Mersmann A, Fill B, Hartmann R, Maurer S. The potential of energy saving by gas-phase adsorption processes. *Chem Eng Technol*. 2000;23(11):937-944. doi:10.1002/1521-4125(200011)23:11<937::AID-CEAT937>3.0.CO;2-P
31. Liang W, Xu F, Zhou X, et al. Ethane selective adsorbent Ni (bdc)(ted) 0.5 with high uptake and its significance in adsorption separation of ethane and ethylene. *Chem Eng Sci*. 2016;148:275-281. doi:10.1016/j.ces.2016.04.016
32. Wu H, Chen Y, Lv D, et al. An indium-based ethane-trapping MOF for efficient selective separation of C_2H_6/C_2H_4 mixture. *Sep Purif Technol*. 2019;212:51-56. doi:10.1016/j.seppur.2018.11.005
33. Newport K, Baamran K, Rownaghi AA, Rezaei F. Magnetic-field assisted gas desorption from Fe_2O_3/zeolite 13X sorbent monoliths for biogas upgrading. *Ind Eng Chem Res*. 2022;61:18843-18853. doi:10.1021/acs.iecr.2c02969
34. Chen DL, Wang N, Wang FF, et al. Utilizing the gate-opening mechanism in ZIF-7 for adsorption discrimination between N_2O and CO_2. *J Phys Chem C*. 2014;118(31):17831-17837. doi:10.1021/jp5056733
35. Thakkar H, Al-Naddaf Q, Legion N, et al. Adsorption of ethane and ethylene over 3d-printed ethane-selective monoliths. *ACS Sustain Chem Eng*. 2018;6(11):15228-15237. doi:10.1021/acssuschemeng.8b03685
36. Lawson S, Baamran K, Newport K, Rezaei F, Rownaghi A. Screening of adsorbent/catalyst composite monoliths for carbon capture-utilization and ethylene production. *ACS Appl Mater Interfaces*. 2021;13(46):55198-55207. doi:10.1021/acsami.1c17668
37. Lawson S, Baamran K, Newport K, et al. Integrated direct air capture and oxidative dehydrogenation of propane with CO_2 at isothermal conditions. *Appl Catal B*. 2022;303(2021):120907. doi:10.1016/j.apcatb.2021.120907
38. Lawson S, Baamran K, Newport K, Rezaei F, Rownaghi AA. Formulation and processing of dual functional adsorbent/catalyst structured monoliths using an additively manufactured contactor for direct capture/conversion of CO_2 with cogeneration of ethylene. *Chem Eng J*. 2022;431(P3):133224. doi:10.1016/j.cej.2021.133224
39. Baamran K, Rownaghi AA, Rezaei F. Direct synthesis of ethylene and hydrogen from CO_2 and ethane over a bifunctional structured CaO/-Cr_2O_3-V_2O_5/ZSM-5 adsorbent/catalyst monolith. *ACS Sustain Chem Eng*. 2022;11(3):1006-1018. doi:10.1021/acssuschemeng.2c05627

40. Baamran K, Lawson S, Rownaghi AA, Rezaei F. Process evaluation and kinetic analysis of 3D-printed monoliths comprised of CaO and Cr/H-ZSM-5 in combined CO_2 capture-C_2H_6 oxidative dehydrogenation to C_2H_4. *Chem Eng J*. 2022;435:134706. doi:10.1016/j.cej.2022.134706
41. Lawson S, Baamran K, Newport K, et al. Adsorption-enhanced bifunctional catalysts for in situ CO_2 capture and utilization in propylene production: a proof-of-concept study. *ACS Catal*. 2022;12(22):14264-14279. doi:10.1021/acscatal.2c04455
42. Thakkar H, Lawson S, Rownaghi AA, Rezaei F. Development of 3D-printed polymer-zeolite composite monoliths for gas separation. *Chem Eng J*. 2018;348(April):109-116. doi:10.1016/j.cej.2018.04.178
43. Al-Naddaf Q, Rownaghi AA, Rezaei F. Multicomponent adsorptive separation of CO_2, CO, CH_4, N_2, and H_2 over core-shell zeolite-5A@MOF-74 composite adsorbents. *Chem Eng J*. 2020;384:123251. doi:10.1016/j.cej.2019.123251
44. Wu X, Shahrak M, Yuan B. Synthesis and characterization of zeolitic imidazolate framework ZIF-7 for CO_2 and CH_4 separation. *Microporous Mesoporous Mater*. 2014;190:189-196.
45. Rashidi F, Blad C, Jones C, Nair S. Synthesis, characterization, and tunable adsorption and diffusion properties of hybrid ZIF-7-90 frameworks. *AIChE J*. 2016;62(2):525-537. doi:10.1002/aic.15102
46. Yang X, Arami-Niya A, Xiao G, May E. Flexible adsorbents at high pressure: observations and correlation of ZIF-7 stepped sorption isotherms for nitrogen, argon, and other gases. *Langmuir*. 2020;36(49):44. doi:10.1021/acs.langmuir.0c02279
47. Baamran K, Moreno JDL, Rownaghi AA, Rezaei F. Kinetic assessment of light hydrocarbons separation over Fe-doped 13X composite sorbents under multicomponent feed conditions. *Ind Eng Chem Res*. 2023;62(30):11917-11929. doi:10.1021/acs.iecr.3c00620
48. Chen SJ, Zhu M, Fu Y, Huang YX, Tao ZC, Li WL. Using 13X, LiX, and LiPdAgX zeolites for CO_2 capture from post-combustion flue gas. *Appl Energy*. 2017;191:87-98. doi:10.1016/j.apenergy.2017.01.031
49. Wu H, Hao L, Chen C, Zhou J. Superhydrophobic Fe_3O_4/OA magnetorheological fluid for removing oil slick from water surfaces effectively and quickly. *ACS Omega*. 2020;5(42):27425-27432. doi:10.1021/acsomega.0c03857
50. Zhuang L, Zhang W, Zhao Y, Shen H, Lin H, Liang J. Preparation and characterization of Fe_3O_4 particles with novel nanosheets morphology and magnetochromatic property by a modified solvothermal. *Sci Rep*. 2015;5:9320 Accessed December 14, 2023. https://www.nature.com/articles/srep09320
51. Morris W, He N, Ray KG, et al. A combined experimental-computational study on the effect of topology on carbon dioxide adsorption in zeolitic imidazolate frameworks. *J Phys Chem C*. 2012;116(45):24084-24090. doi:10.1021/jp307170a
52. He M, Yao J, Li L, Wang K, Chen F, Wang H. Synthesis of zeolitic imidazolate framework-7 in a water/ethanol mixture and its ethanol-induced reversible phase transition. *ChemPlusChem*. 2013;78(10):1222-1225. doi:10.1002/cplu.201300193
53. Cuadrado-Collados C, Fernández-Català J, Fauth F, et al. Understanding the breathing phenomena in nano-ZIF-7 upon gas adsorption. *J Mater Chem A Mater*. 2017;5(39):20938-20946. doi:10.1039/C7TA05922A
54. Van Miltenburg A, Zhu W, Kapteijn F, Moulijn JA. Adsorptive separation of light olefin/paraffin mixtures. *Chem Eng Res Design*. 2006;84(5):350-354. doi:10.1205/cherd05021
55. Hartmann M, Böhme U, Hovestadt M, Paula C. Adsorptive separation of olefin/paraffin mixtures with ZIF-4. *Langmuir*. 2015;31(45):12382-12389. doi:10.1021/acs.langmuir.5b02907
56. Lawson S, Adebayo B, Robinson C, Al-Naddaf Q, Rownaghi AA, Rezaei F. The effects of cell density and intrinsic porosity on structural properties and adsorption kinetics in 3D-printed zeolite monoliths. *Chem Eng Sci*. 2020;218(15):7151-7160. doi:10.1016/j.ces.2020.115564

SUPPORTING INFORMATION

Additional supporting information can be found online in the Supporting Information section at the end of this article.

How to cite this article: Baamran K, Shareef U, Rezaei F. Induction vacuum swing adsorption over magnetic sorbent monoliths and extrudates for ethylene/ethane separation. *AIChE J*. 2024;70(7):e18401. doi:10.1002/aic.18401